International Journal of Heat and Mass Transfer 52 (2009) 680–693

Contents lists available at ScienceDirect

International Journal of Heat and Mass Transfer

journal homepage: www.elsevier.com/locate/ijhmt

Simulation of turbulent impinging jet into a cylindrical chamber with and without a porous layer at the bottom

Daniel R. Graminho, Marcelo J.S. de Lemos *

Departamento de Energia - IEME, Instituto Tecnológico de Aeronáutica - ITA, 12228-900 - São José dos Campos - SP, Brazil

ARTICLE INFO

Article history:
Received 4 February 2008
Received in revised form 8 July 2008
Available online 24 September 2008

Keywords:
Turbulent flow
Porous media
Numerical methods
Impinging jet
Modeling

ABSTRACT

Turbulent impinging jets on heated surfaces are widely used in industry to modify local heat transfer coefficients. The addition of a porous substrate covering the surface contributes to a better flow distribution, which favors many engineering applications. Motivated by this, this work shows numerical results for a turbulent impinging jet into a cylindrical enclosure with and without a porous layer at the bottom. The macroscopic time-averaged equations for mass and momentum are obtained based on a concept called double decomposition, which considers spatial deviations and temporal fluctuations of flow properties. Turbulence is handled with a macroscopic k–ε model, which uses the same set of equations for both the fluid layer and the porous matrix. The numerical technique employed is the control volume method in conjunction with a boundary-fitted coordinate system. One unique computational grid is used to compute the entire heterogeneous medium. The SIMPLE algorithm is applied to relax the system of algebraic equations. Results indicate that the permeability of the porous layer and the height of the fluid layer significantly affect the flow pattern. The effect of the porous layer thickness was less pronounced in affecting the flow behavior in the fluid layer.

1. Introduction

Impinging jets are flow systems where an ejector is used to create a high-speed flow colliding against an obstacle. Near the stagnation point, velocity gradients tend to be high favoring localized mass and heat transfer mechanisms. As such, these jets are widely used in industry, mostly as devices to promote and control localized heat and mass transfer rates. Common industrial applications for impinging jets are cooling of metals in steel industry, glass tempering and ventilation of electrical components. Since the majority of applications uses air and water as the cooling fluid due to their relatively low viscosity, flow velocity tends to be high and the study of impinging jets in turbulent regime becomes necessary.

Most studies about turbulent impinging jets available in the literature refer to heat transfer obtained with a coolant flowing through a clear medium (non-porous), before reaching a surface. Two-dimensional jets in laminar regime are investigated in Law et al. [1], who made an extensive numerical analysis of the hydrodynamic characteristics of a 2D jet impinging normally against a flat plate. They found differences in the size of the recirculating bubble depending on the length of the confining plates. Baydar [2] experimentally evaluated the hydrodynamics characteristics of single and double jets colliding against a plate. Chalupa et al. [3] analyzed the mass transfer induced by a bidimensional turbulent jet and Park et al. [4] made a comparison between different numerical methods in flow resolution for both laminar and turbulent regimes.

The study of transport phenomena in porous media is relatively new. In the last decade, a number of analyses were published in the literature due to its great potential for innovative technological applications. For example, thermal performance of porous media was studied by Vafai et al. [5] evaluating the heat transfer of a hybrid medium. Huang and Vafai [6] investigated the heat transfer of a flat plate covered with a porous insert. Effects of the insertion of a porous medium in a fluid stream were evaluated by Hadim [7], who investigated the flow of a channel both fully and partially filled with a porous insert. In the recent years, a number of papers have been published covering a very wide range of problems involving flow and heat transfer in permeable media [8–17], including flows parallel to a layer of porous material [18] and across baffles made of permeable media [19,20].

Investigation on configurations concerning perpendicular jets into a porous core is much needed for optimization of heat sinks attached to solid surfaces. However, studies of porous medium under impinging jets are yet very scarce in the literature. Examples of this kind of work are in Prakash et al. [21,22], who presented an experimental and numerical study of turbulent jets impinging on a porous layer. Fu et al. [23] evaluated the thermal performance of different porous media under an impinging jet. Another example is of numerical simulations by Kim & Kuznetsov [24], who investigated optimal characteristics of impinging jets into heat sinks. Re-

* Corresponding author. Tel.: +55 12 3947 5860; fax: +55 12 3947 5842.
E-mail address: delemos@ita.br (M.J.S. de Lemos).

0017-9310/$ - see front matter © 2008 Elsevier Ltd. All rights reserved.
doi:10.1016/j.ijheatmasstransfer.2008.07.044

Nomenclature

Latin characters

c_1	Non-dimensional turbulence model constant
c_2	Non-dimensional turbulence model constant
c_F	Forchheimer coefficient
c_k	Non-dimensional turbulence model constant
c_μ	Non-dimensional turbulence model constant
D	Collision plate diameter
D_j	Jet nozzle diameter
H	Clear medium height
H_c	Height of main recirculating bubble
h_p	Porous layer height
K	Permeability of the porous medium
k	Turbulence kinetic energy per mass unit, $k = \overline{\mathbf{u}' \cdot \mathbf{u}'}/2$
$\langle k \rangle^i$	k intrinsic average
R	Radius of cylindrical chamber
R_c	Radius of main recirculating bubble
r/R	Dimensionless radial position
w	Exit flow ring length
z	Axial distance from collision plate
z/H	Dimensionless axial distance from collision plate

Greek characters

ε	Dissipation rate of k
$\langle \varepsilon \rangle^i$	Intrinsic average of ε
ϕ	$\phi = \Delta V_f / \Delta V$, Porosity
μ	Dynamic viscosity
$\mu_{t\phi}$	Macroscopic turbulent viscosity
ρ	Density
σ_k	Non-dimensional constant
σ_ε	Non-dimensional constant
σ_T	Non-dimensional constant
τ_w	Wall shear stress, $\tau_w = \mu \frac{du}{dy}$

Special characters

φ	General variable
$\bar{\varphi}$	Time average
φ'	Time fluctuation
$\langle \varphi \rangle^i$	Intrinsic average

cently, Saeld, N.H [25] presented computations for laminar flow of a jet entering a porous layer. He investigated the effect of cross flow on heat transfer characteristics.

This work uses the methodology proposed by Pedras and de Lemos [27,28], who developed a macroscopic two-equation model for turbulent flow in permeable matrices. The problem of turbulent flow parallel to a layer of porous material was later investigated by de Lemos [29] and de Lemos and Silva [30]. Recently, in an accompanying paper [31], laminar normally imping jets onto a flat layer of porous medium were studied, aiming at contributing to the understanding of flow structure in that configuration. Such flow cases, concerning perpendicular turbulent jets into a porous core, are much needed for optimization of heat sinks attached to solid surfaces. To this end, this contribution extends the work in [31], considering now turbulent flow regime simulated with the macroscopic k–ε model of [27,28].

2. Geometry and physical system

The problem considered is schematically presented in Fig. 1a, which shows the same geometry used by Prakash et al. [21,22]. The reason for choosing the same geometry as in the pioneering work of [21,22] was to be able to validate the computations herein with the experimental data provided by them. As shown in the figure, a fluid jet enters a cylindrical chamber through an aperture in an upper disk. An annular clearance between the cylinder lateral wall and the disc allows fluid to flow out of the enclosure. The incoming jet diameter, D_j, is 0.019 m and the inner cylinder diameter, D, is 0.39 m. The clearance between the cylinder and the disc holding the jet has a width, w, equal to 0.005 m. At the bottom of the chamber, a layer of porous material covers the surface and is hit by the incoming jet. Three different heights of fluid column above the porous substrate, H, namely 0.05 m, 0.1 m and 0.15 m, were used in the simulations. Two thicknesses of the porous layer, h_p, were considered, namely 0.05m and 0.1 m. The average velocity of the incoming jet was 1.6 m/s representing a Reynolds number of 30,000, which was based on the jet exit diameter. Different velocities were also used when evaluating the influence of Reynolds number on the main flow. The two other values 1.0 and 2.5 m/s corresponded to Re = 18,900 and 47,000, respectively. Turbulent results for streamfunction, velocity and turbulence kinetic energy profiles are compared here with those from Prakash et al. [21,22].

3. Mathematical model

Before continuing, a word about the class of turbulence model applied here seems timely. The mathematical framework for treating turbulent flow in porous media, used in this work, is based on a macroscopic version of the standard k–ε model of Jones and Launder (1972) [26]. It is well known in the literature, for nearly two decades, the shortcomings and limitations of the k–ε in predicting separation over curved surfaces, size of recirculation bubbles in sudden expansions/contractions and in flows subjected to strong normal strains, as in impinging jets onto solid surfaces. All of these examples, however, refer to free flows with no porous body embedded into the domain of calculation. Accordingly, the objective here was twofold. First, to simulate the flow in Fig. 1 with one unique set of equations, valid for both the porous substrate and the fluid layer. Secondly, to use a mathematical framework that has the characteristics of easy of programming in existing codes and the desirable advantages of numerical robustness and stability, which is obtained via the diffusion-like stress-strain relation inherent to the k–ε model. For these reasons, the two-equation model of [26], which was extended to hybrid media (free/porous regions) by [27], is used here. Also, further justification for using the k–ε level of closure in the flow of Fig. 1 is presented in Prakash et al. [21].

As mentioned, the mathematical model here used takes into account a systematic development presented in a series of papers already available in the open literature [27–30], where all equations and their mathematical derivations can be found. Therefore, these equations will be just reproduced here and details about their derivations can be obtained in the mentioned papers. In addition, the development in [27–30], has been extended to non-buoyant heat transfer under local thermal equilibrium [32,33], buoyant flows [34–41], mass transfer [42] and double diffusion [43], including applications to channel with porous inserts [44] and moving porous beds [45,46]. In that development, it was assumed that the porous matrix was homogeneous, rigid, steady and saturated by an incompressible fluid. Also, all physical properties were kept constant.

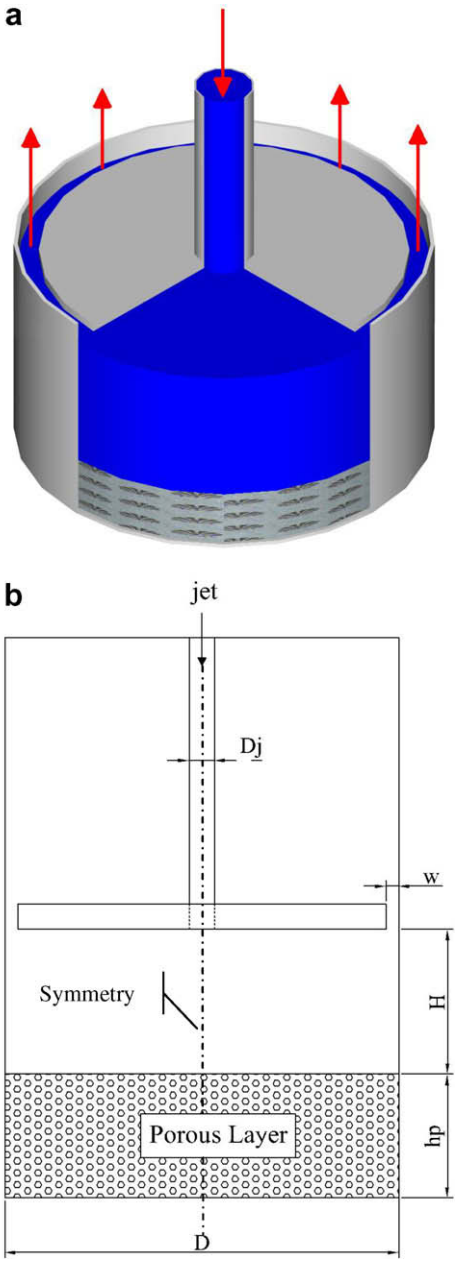

Fig. 1. Geometry: (a) confined jet impinging against a porous layer, (b) cross section view and nomenclature.

3.1. Macroscopic continuity equation

The macroscopic continuity equation can be written as

$$\nabla \cdot \bar{\mathbf{u}}_D = 0 \tag{1}$$

where $\bar{\mathbf{u}}_D$ is the average surface velocity (also known as Darcy velocity). In Eq. (1) the Dupuit-Forchheimer relationship, $\bar{\mathbf{u}}_D = \phi\langle\bar{\mathbf{u}}\rangle^{\mathrm{i}}$, has been used, where ϕ is the porous medium porosity and $\langle\bar{\mathbf{u}}\rangle^{\mathrm{i}}$ identifies the intrinsic average of fluid velocity $\bar{\mathbf{u}}$ (Gray and Lee (1977) [47].

3.2. Macroscopic momentum and turbulence equations

The macroscopic momentum equation is given by,

$$\rho\left[\frac{\partial\bar{\mathbf{u}}_D}{\partial t} + \nabla\cdot\left(\frac{\bar{\mathbf{u}}_D\bar{\mathbf{u}}_D}{\phi}\right)\right] = -\nabla\left(\phi\langle\bar{p}\rangle^{\mathrm{i}}\right) + \mu\nabla^2\bar{\mathbf{u}}_D + \nabla\cdot\left(-\rho\phi\langle\overline{\mathbf{u}'\mathbf{u}'}\rangle^{\mathrm{i}}\right) - \left[\frac{\mu\phi}{K}\bar{\mathbf{u}}_D + \frac{c_F\phi\rho|\bar{\mathbf{u}}_D|\bar{\mathbf{u}}_D}{\sqrt{K}}\right] \tag{2}$$

where $-\rho\phi\langle\overline{\mathbf{u}'\mathbf{u}'}\rangle^{\mathrm{i}}$ is the macroscopic Reynolds Stress Tensor, given by:

$$-\rho\phi\langle\overline{\mathbf{u}'\mathbf{u}'}\rangle^{\mathrm{i}} = \mu_{t_\phi}2\langle\bar{\mathbf{D}}\rangle^{\mathbf{v}} - \frac{2}{3}\phi\rho\langle k\rangle^{\mathrm{i}}\mathbf{I} \tag{3}$$

where

$$\langle\bar{\mathbf{D}}\rangle^{v} = \frac{1}{2}\left[\nabla(\phi\langle\bar{\mathbf{u}}\rangle^{\mathrm{i}}) + [\nabla(\phi\langle\bar{\mathbf{u}}\rangle^{\mathrm{i}})]^T\right] \tag{4}$$

is the macroscopic deformation rate, $\langle k^{\mathrm{i}}\rangle$ is the intrinsic turbulent kinetic energy per mass unit and μ_{t_ϕ} is the macroscopic turbulent viscosity, defined as:

$$\mu_{t_\phi} = \rho c_\mu\frac{\langle k\rangle^{\mathrm{i}^2}}{\langle\varepsilon\rangle^{\mathrm{i}}} \tag{5}$$

where c_μ is a constant. In order to calculate μ_{t_ϕ}, information on $\langle k\rangle^{\mathrm{i}} = \langle\overline{\mathbf{u}'}\cdot\mathbf{u}'\rangle^{\mathrm{i}}/2$ and $\langle\varepsilon\rangle^{\mathrm{i}} = \mu\langle\overline{\nabla\mathbf{u}'}:(\nabla\mathbf{u}')^T\rangle^{\mathrm{i}}/\rho$ distributions are needed. These quantities are obtained from transport equations, which read,

$$\rho\left[\frac{\partial}{\partial t}\left(\phi\langle k\rangle^{\mathrm{i}}\right) + \nabla\cdot\left(\bar{\mathbf{u}}_D\langle k\rangle^{\mathrm{i}}\right)\right] = \nabla\cdot\left[\left(\mu + \frac{\mu_{t_\phi}}{\sigma_k}\right)\nabla\left(\phi\langle k\rangle^{\mathrm{i}}\right)\right] - \rho\langle\overline{\mathbf{u}'\mathbf{u}'}\rangle^{\mathrm{i}} : \nabla\bar{\mathbf{u}}_D + c_k\rho\frac{\phi\langle k\rangle^{\mathrm{i}}|\bar{\mathbf{u}}_D|}{\sqrt{K}} - \rho\phi\langle\varepsilon\rangle^{\mathrm{i}} \tag{6}$$

$$\rho\left[\frac{\partial}{\partial t}\left(\phi\langle\varepsilon\rangle^{\mathrm{i}}\right) + \nabla\cdot\left(\bar{\mathbf{u}}_D\langle\varepsilon\rangle^{\mathrm{i}}\right)\right] = \nabla\cdot\left[\left(\mu + \frac{\mu_{t_\phi}}{\sigma_\varepsilon}\right)\nabla\left(\phi\langle\varepsilon\rangle^{\mathrm{i}}\right)\right] + c_1\left(-\rho\langle\overline{\mathbf{u}'\mathbf{u}'}\rangle^{\mathrm{i}} : \nabla\bar{\mathbf{u}}_D\right)\frac{\langle\varepsilon\rangle^{\mathrm{i}}}{\langle k\rangle^{\mathrm{i}}} + c_2c_k\rho\frac{\phi\langle\varepsilon\rangle^{\mathrm{i}}|\bar{\mathbf{u}}_D|}{\sqrt{K}} - c_2\rho\phi\frac{\langle\varepsilon\rangle^{\mathrm{i}^2}}{\langle k\rangle^{\mathrm{i}}} \tag{7}$$

where c_k, σ_k, c_1 andc_2 constants.

Further, constants of the standard k-ε turbulence model in Eqs. (5)–(7), according to Launder & Spalding (1974) [51] are given by:

$$c_\mu = 0.09, c_1 = 1.44, c_2 = 1.92, \sigma_k = 1.0, \sigma_\varepsilon = 1.33$$

4. Boundary and interface conditions

At the jet exit, a fully developed profile for velocity, k and ε was imposed. At the flow outlet through the clearance of width w, a zero diffusion flux condition was set. On the walls, a non-slip condition was applied and at the centerline of the cylinder, the symmetry condition was used.

At the interface between the porous layer and the clear region the macroscopic velocity, intrinsic pressure, turbulence kinetic energy and its dissipation rate, as well as their respective diffusive fluxes, were assumed to be continuous functions so that,

$$\bar{\mathbf{u}}_D|_{0<\phi<1} = \bar{\mathbf{u}}_D|_{\phi=1} \tag{8}$$

$$\langle\bar{p}\rangle^{\mathrm{i}}\Big|_{0<\phi<1} = \langle\bar{p}\rangle^{\mathrm{i}}\Big|_{\phi=1} \tag{9}$$

$$\langle k\rangle^{v}|_{0<\phi<1} = \langle k\rangle^{v}|_{\phi=1} \tag{10}$$

$$\left(\mu + \frac{\mu_{t_\phi}}{\sigma_k}\right)\frac{\partial\langle k\rangle^{v}}{\partial y}\Big|_{0<\phi<1} = \left(\mu + \frac{\mu_t}{\sigma_k}\right)\frac{\partial\langle k\rangle^{v}}{\partial y}\Big|_{\phi=1} \tag{11}$$

$$\langle\varepsilon\rangle^{v}|_{0<\phi<1} = \langle\varepsilon\rangle^{v}|_{\phi=1} \tag{12}$$

$$\left(\mu + \frac{\mu_{t_\phi}}{\sigma_\varepsilon}\right)\frac{\partial\langle\varepsilon\rangle^{v}}{\partial y}\Big|_{0<\phi<1} = \left(\mu + \frac{\mu t}{\sigma_\varepsilon}\right)\frac{\partial\langle\varepsilon\rangle^{v}}{\partial y}\Big|_{\phi=1} \tag{13}$$

5. Numerical details

Due to the symmetry condition at the cylinder center (see Fig. 1b), the computational domain adopted covered only half of

the vertical cylinder cross section. Equations were solved for axi-symmetric flow and, as such, no flow asymmetries were considered. Further, simulations were carried out using only a High Reynolds number turbulence model, which considers wall-functions for representing the flow in the proximity of the wall instead of computing the velocity field through the buffer and laminar sub-layers (Launder & Spalding (1974) [51]).

The method utilized to numerically solve the flow equations was the finite volume method applied to a boundary-fitted coordinate system. Equations were discretized in a two-dimensional control volume involving both the clear and the porous medium. For solving the algebraic equation set, the SIMPLE algorithm was used (Patankar (1980) [48]) and normalized residues for the transport equations were brought down to 10^{-6}. The interface was positioned to coincide with the border between two adjacent control volumes, generated in such a way that volumes are either "totally porous" or "totally clear". Details of the numerical implementation can be found in de Lemos and Silva (2006) [30].

Grid independence studies were conducted using meshes with 50×50, 100×100 and 200×200 computational nodes, which were distributed non-uniformly in the flow domain. Mesh independence tests were carried out utilizing the friction factor at the walls as the evaluation parameter. No significant deviation (differences of less than 1%) could be detected comparing the 100×100 and the 200×200 grids. As such, all simulations herein adopted the 100×100 mesh.

6. Results and discussion

First, for code validation, initial simulations were conducted in the clear chamber of height H, where free flow occurs (Fig. 1b). This first set of simulations considers that a solid wall is located at depth H and no porous layer is positioned at the bottom of the chamber. Therefore, streamlines, velocity profiles and turbulence kinetic energy contours for an empty enclosure are presented prior to showing computations considering the porous layer in Fig. 1a. Also, for convenience in presenting results, all figures below, which contain streamline patterns, are plotted with the symmetry axis aligned with the horizontal direction, with the jet coming at the lower left corner of the figures.

Also, it is important to emphasize the main differences of the work herein and that presented by Prakash et al. [21]. Here, the turbulence model used is composed by only one set of equations and is applied without any distinction within the fluid layer and the porous material. These equations are (1), (2), (6) and (7). In Prakash et al (2001 [21], the model of Antohe and Lage (1997) [49] was applied, which is based on a volume-time sequence of integration of local instantaneous equations. In addition, more than one set of equations were used in [21], with different combinations of distinct terms in their modeled k-equation. Besides, a closure where the flow was assumed laminar within the porous matrix was also considered in [21]. Here, only one model is employed to handle turbulence, regardless if the computation node lies in the free flow region or in the porous matrix.

Further, the mathematical closure here employed follows the work of Pedras and de Lemos (2001) [27], which used the reversed order of integration (time-volume sequence) for obtaining the set of transport equations. The relationship between these two models is explained by a new concept named double-decomposition. The interested reader is referred to de Lemos (2005) [50] where more information on such concept can be found.

Therefore, besides the use of a different numerical technique, with one single computation grid for the entire computational domain, the work herein makes use of a model that needs no adjustments if it is applied in free flow regions (fluid layer) or in the porous substrate. Having the distinction between such two approaches been clarified, the sections below present simulations for a clear chamber and for the case where a porous material is positioned at the bottom of the cylinder shown in Fig. 1.

7. Clear chamber

7.1. Mean flow

Fig. 2 shows a comparison of the numerically simulated streamfunctions with experimental flow visualizations and CFD results from Prakash et al. [21] for $H = 0.15$ m. For this case, the entire half plane of the cylinder is filled with one large recirculation cell. A small secondary recirculation bubble can be seem in the top-right corner of the picture, but with negligible dimensions compared to the main one. Simulations seem to be close to literature results, with main flow streamlines following very closely the pattern given by the LDV experiments. Also, the flow in the core region and close to the walls agrees well with available CFD results, indicating that simulations herein may well represent actual flow behavior within the entire chamber.

The effect of the fluid layer height, H, given in Fig. 3 shows the streamfunctions for $H = 0.15$, 0.10 and 0.05 m. By decreasing the liquid height, main flow behavior remains the same, with a central dominant recirculation. The peripheral recirculations get smaller

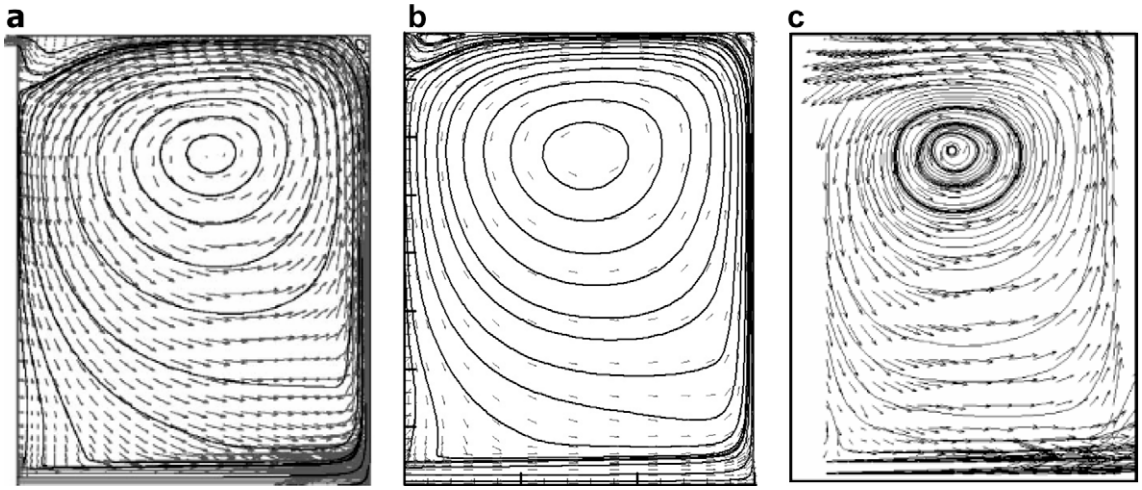

Fig. 2. Comparison of streamfunctions for $Re = 3000$, $H = 0.15$ m: (a) CFD Results – Prakash et al. (2001), (b) present results, (c) LDV Measurements – Prakash et al. (2001).

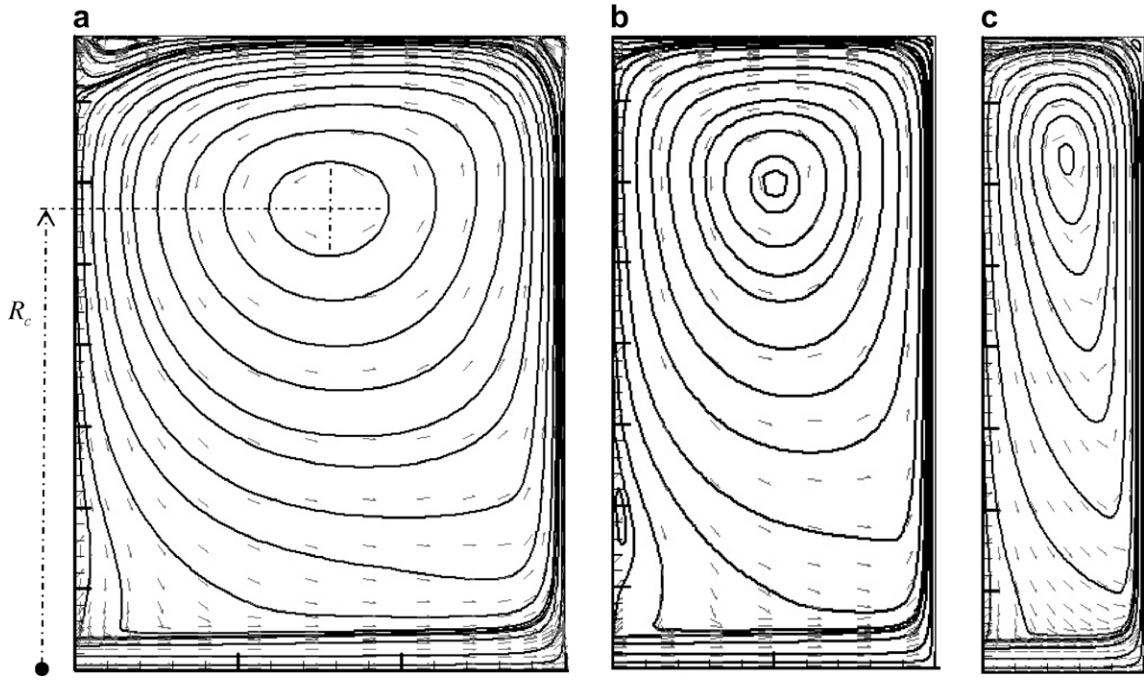

Fig. 3. Effect of fluid layer height on streamlines for Re = 30,000. (a) H = 0.15 m, (b) H = 0.10 m, (c) H = 0.05 m.

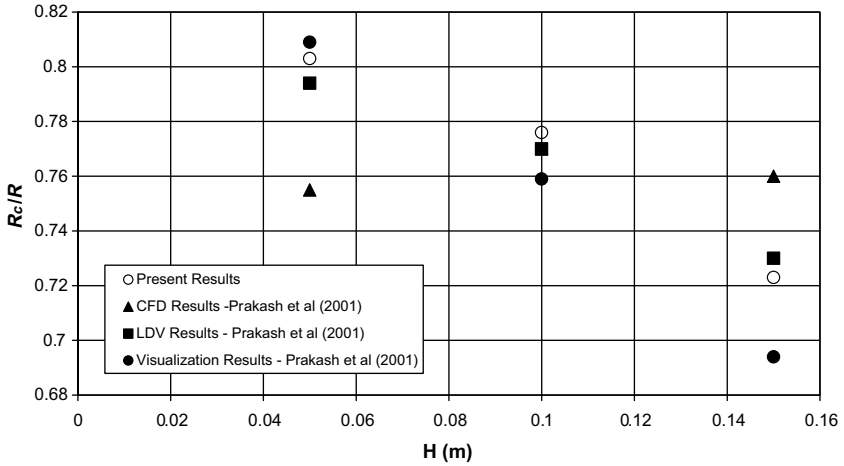

Fig. 4. Radial position of center recirculation as a function of fluid layer height, H.

with the decrease in H. For H = 0.1 m, a recirculation appears close to the jet exit-, and both secondary recirculations close to the cylinder wall are reduced compared to the case with H = 0.15 m. With a further decrease in H, the main recirculation becomes elongated and the peripheral ones nearly vanish.

Fig. 4 shows the horizontal position of the main recirculation for different liquid heights. The R_c/R axis represents the normalized radial position of the recirculation, where R is the radius of the cylindrical chamber. From the picture, it can be seen that the center of the recirculation moves closer to the cylinder wall as H decreases. Present computations seem to follow the trends in both measurement and visualization results, *i.e.*, reduction of R_c as H increases. Fig. 5 gives the influence of Reynolds number on the main flow pattern. It can be seen that a change in Re does not have a significant effect on the main flow pattern. The most noticeable change is a secondary recirculation developing close to the jet exit (lower left corner). With an increase in Reynolds number, such recirculation tends to get smaller up to Re = 30,000. Past this value, the effect of Reynolds number on the flow pattern seems to be small.

Fig. 6 shows the axial velocity profiles for fluid heights equal to 0.15, 0.1 and 0.05 m. In this figure, the profiles have been plotted for six different axial locations covering the entire cylindrical chamber. It can be seen that close to the jet centerline and near the surface at the bottom, results seem to fall in between numerical and experimental data available in the literature. At higher axial distance, present simulations align with CFD predictions in the literature, but both overpredict the axial velocity at the centerline. According to Prakash et al. [22], experimental conditions at inlet did not correspond to fully developed flow, whereas numerical simulations here reported assumed such condition. In general, simulations fail to predict the reduction in the centerline velocity as

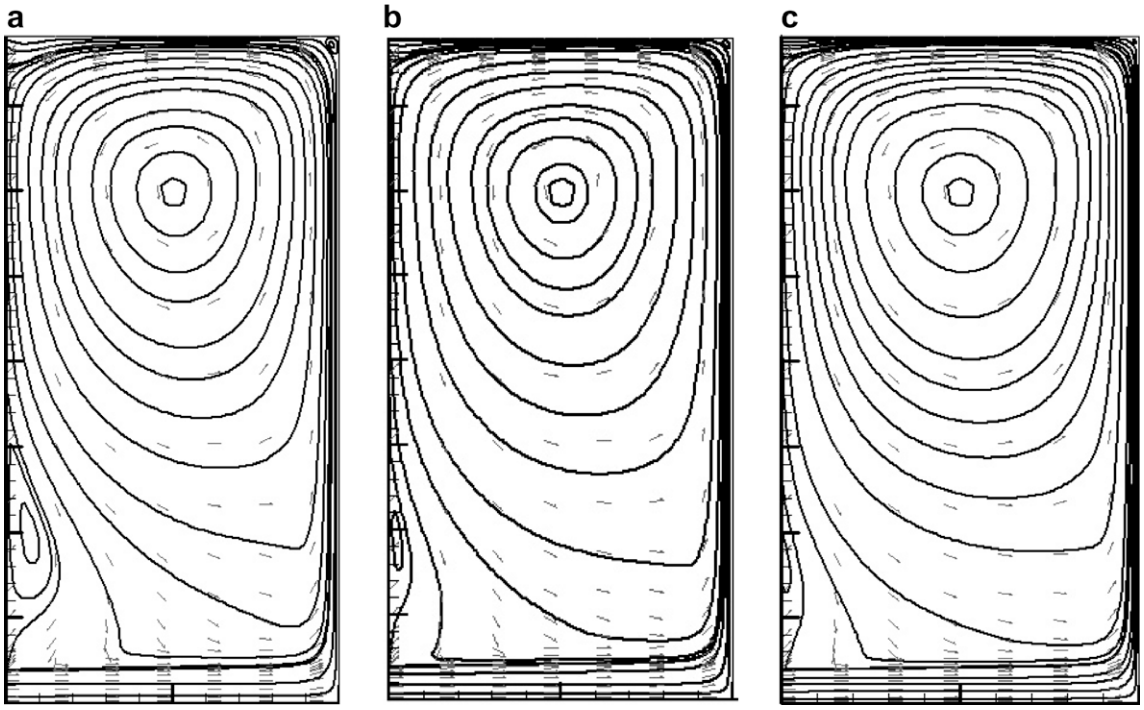

Fig. 5. Effect of Reynolds number on streamfunctions for $H = 0.10$ m: (a) $Re = 18900$, (b) $Re = 30{,}000$, (c) $Re = 47{,}000$.

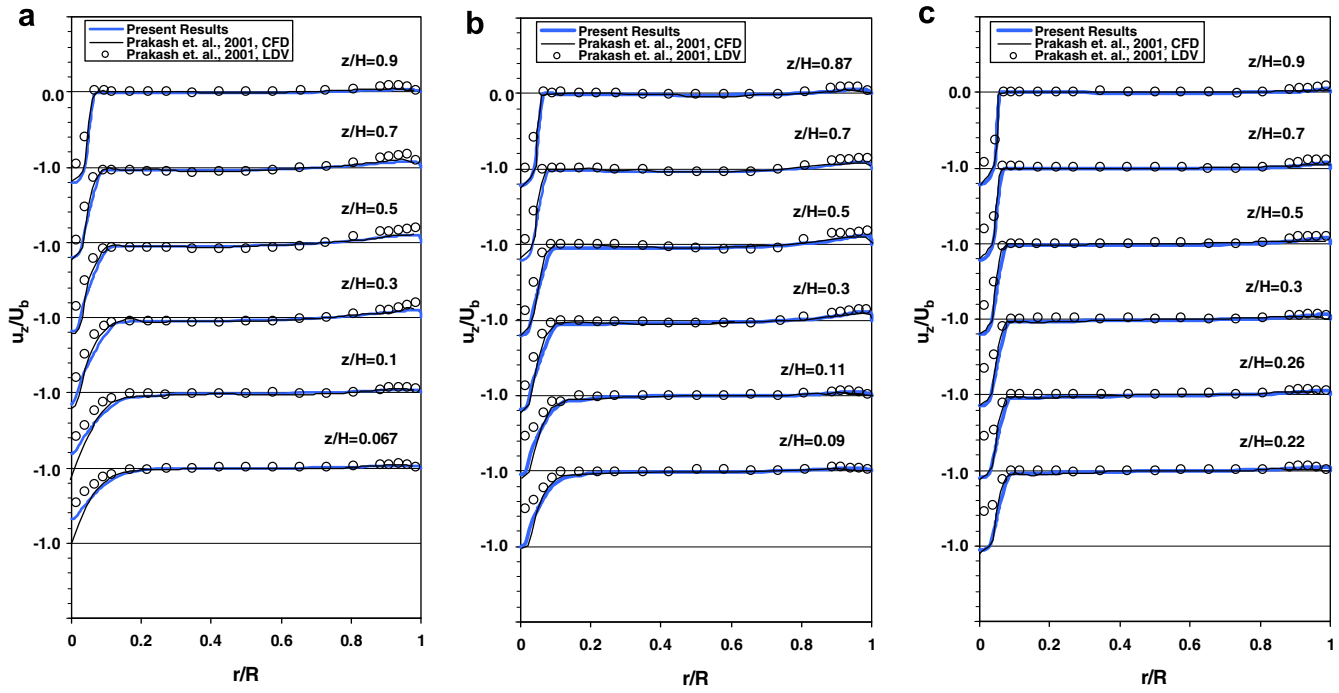

Fig. 6. Axial velocity profiles for cases without foam: (a) $H = 0.15$ m, (b) $H = 0.10$ m, (c) $H = 0.05$ m.

the bottom surface approaches. However, elsewhere in the chamber the main features of the flow were reproduced.

Radial velocity profiles for the three fluid layers investigated are presented in Fig. 7. For $H = 0.15$ m, results follow reasonably well experimental data for $z/H > 0.5$, but underpredicts measured velocities as one gets closer to the plate at the bottom. The same trend is observed in the reported CFD predictions. For $H = 0.10$ m and r/R less than 0.1, computations reproduce the experimental data reasonably well, but in the range $0.1 < r/R < 0.6$ and for lower values of z/H, simulations herein fall above experimental values for velocities. At $H = 0.05$ m, the present curves seem to closely follow the experimental data trend for higher values of z/H. As the flow moves away from the symmetry axis and further down from the jet exit, the quality of predictions seems to deteriorate. Nevertheless, the main features of the flow were captured by the simulations reported here.

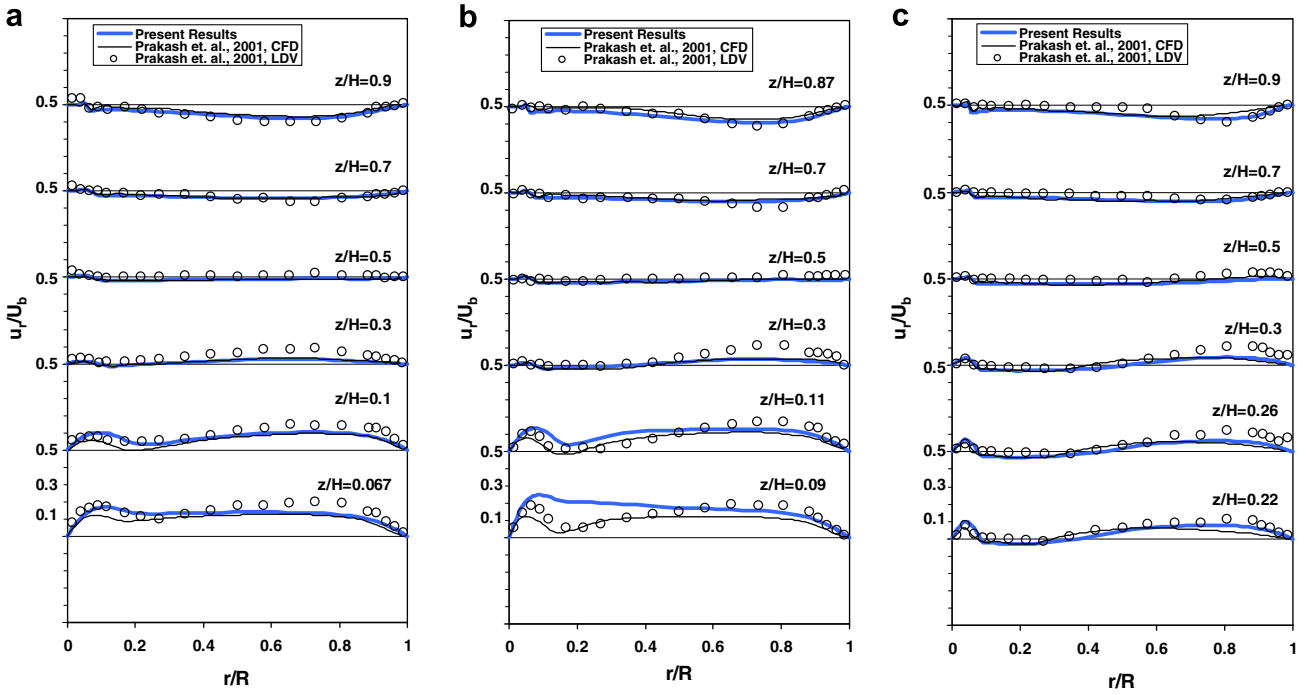

Fig. 7. Radial velocity profiles for cases without foam: (a) $H = 0.15$ m, (b) $H = 0.10$ m, (c) $H = 0.05$ m.

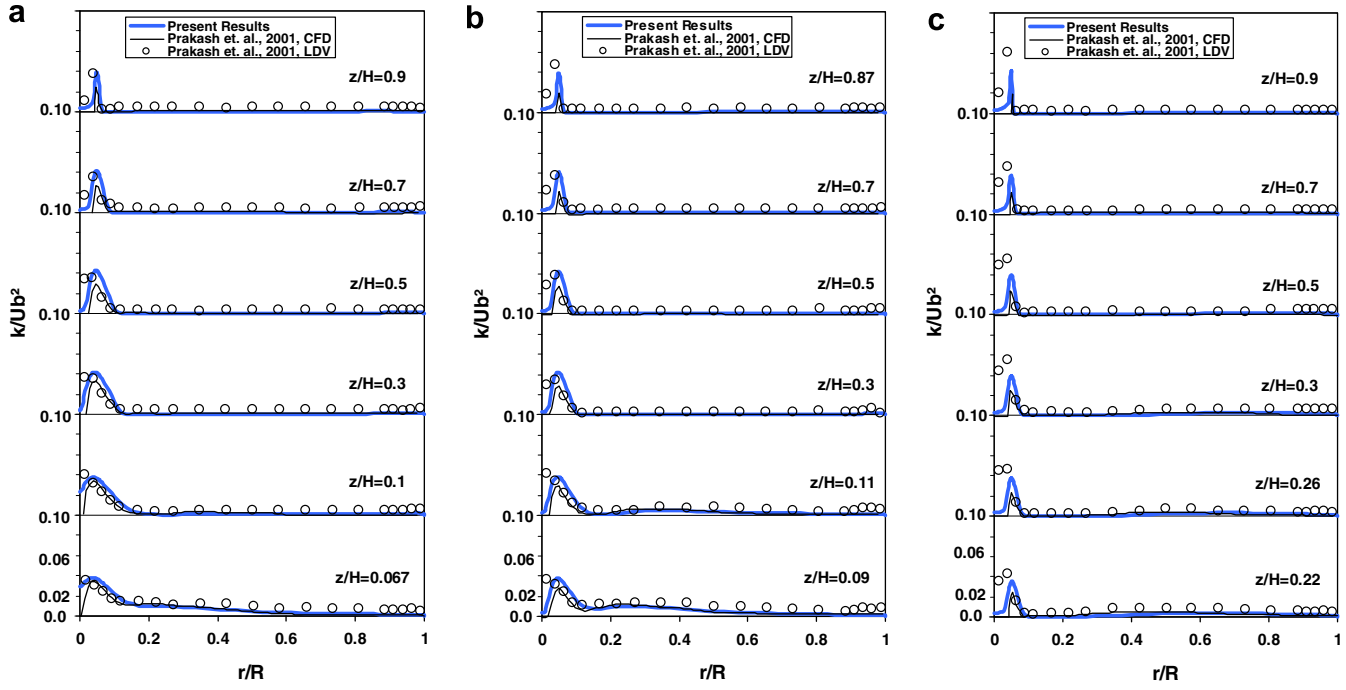

Fig. 8. Turbulence kinetic energy profiles for cases without foam: (a) $H = 0.15$ m, (b) $H = 0.10$ m, (c) $H = 0.05$ m.

7.2. Turbulent field

Fig. 8 shows the turbulence kinetic energy profiles for the same conditions as above. For all fluid layer heights, results reproduce very closely experimental data, including the peak value of k near the symmetry axis, which is caused by the strong shear layer formed around the incoming jet. Close to the impingement plate, a second elevation in turbulence kinetic energy appears. This second maximum is attributed to a laminar-turbulent boundary layer transition in the wall jet region, as defined in Incropera and DeWitt (1990) [52]. That is, the flow decelerates when coming close to the wall, turbulence is damped and the laminar regime prevails in the stagnation region. Afterwards, the flow turns and accelerates along the wall. Overall, simulations herein seem to reproduce basic aspects of the flow pattern, providing the necessary code validation prior to presenting next set of simulations, which include a layer of porous material at the bottom of the chamber.

Before leaving this section, it is important to emphasize that both the present work and simulations by Prakash et al. [21] used turbulence models of the same level (two-equation closure) and that both sets of results reproduced the main features of the experimental data. As already mentioned, in [21] arguments were presented for justifying the use of a k–ε model for this configuration, in spite of the well-established shortcomings of such model. In this work, the same view expressed in Prakash et al. [21] is shared by the authors.

Table 1
Porous medium properties for simulated foams (taken form Prakash et al. (2001a and b) [21,22])

Foam	G10	G30	G45	G60
ϕ	0.971	0.9755	0.978	0.976
K (m^2)	2.84E−7	6.95E−8	1.6E−8	1.2E−8
c (m)	0.1227	0.1218	0.1232	0.1161

8. Porous medium

As mentioned, two different thicknesses h_p were considered for the porous layer at the bottom of the cylinder, namely $h_p = 0.10$ and 0.05 m. Porous medium properties are given in Table 1, where the values are the same as those for metallic porous foams used by Prakash et al. [21,22]. All porosities considered are nearly equal and close to unity, so that the changes on the porous material effectively represent a change in its permeability. Material G10 is the most permeable. According to the nomenclature used in Prakash et al. [21,22], the label for the metallic foams is associated with its number of pores per inch, ppi. Thus, material G10 had 10 pores per inch.

8.1. Mean flow

Fig. 9 shows a comparison of the numerically simulated streamfunctions with experimental flow visualizations and CFD data from Prakash et al. [21,22] for $H = 0.10$ m, $h_p = 0.05$ m and $Re = 30{,}000$ for the porous foam G10. From the picture, the presence of two large recirculationg zones dominating the entire flow can be seen,

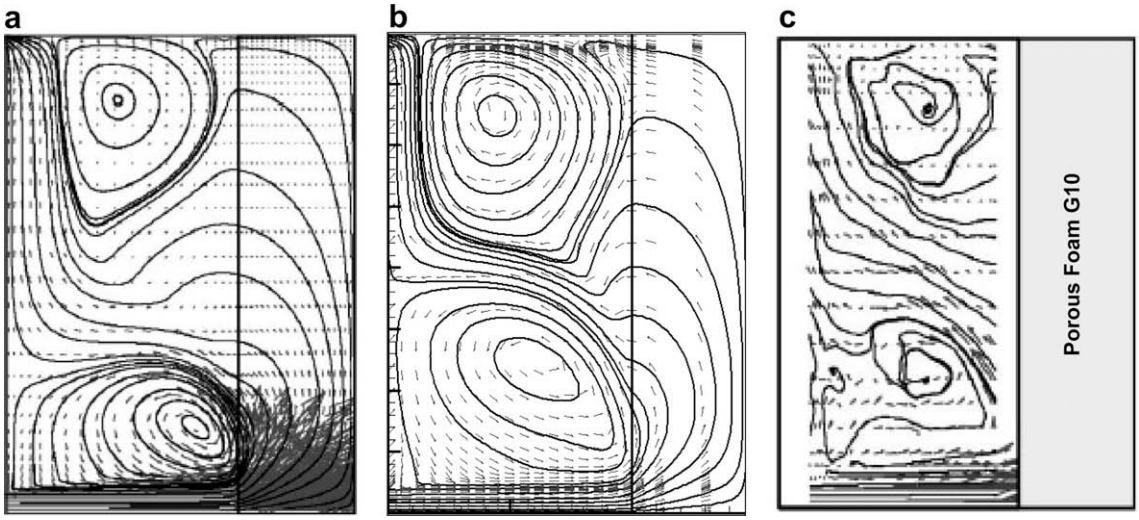

Fig. 9. Comparison of streamfunction pattern for $H = 0.10$ m, $h_p = 0.05$ m and porous foam G10: (a) CFD Results – Prakash et al. (2001), (b) Present Results, (c) LDV Measurements – Prakash et al. (2001).

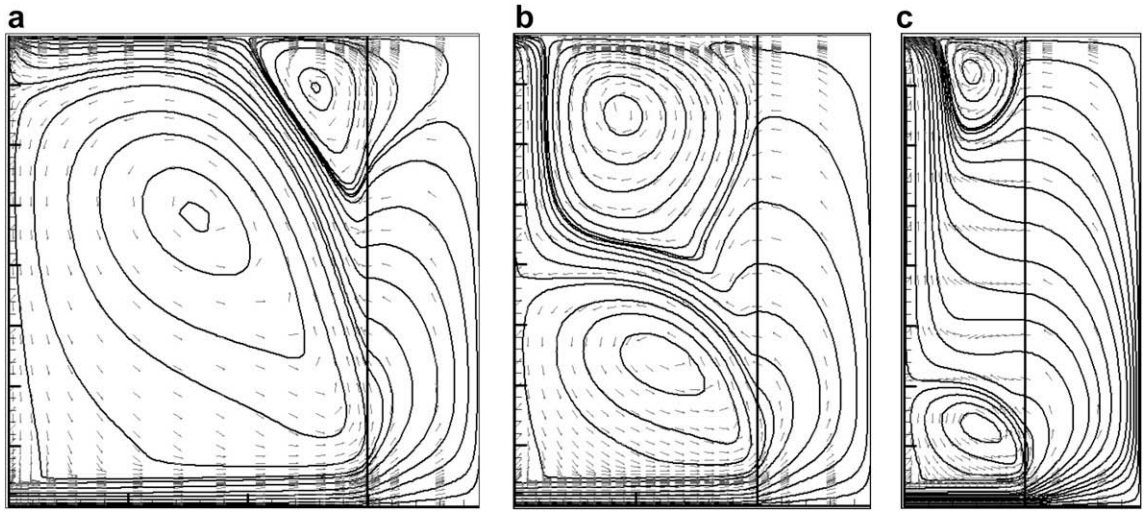

Fig. 10. Effect of the fluid layer height on stream function for $h_p = 0.05$ m, $Re = 30{,}000$ and porous foam G10: (a) $H = 0.15$ m, (b) $H = 0.10$ m, (c) $H = 0.05$ m.

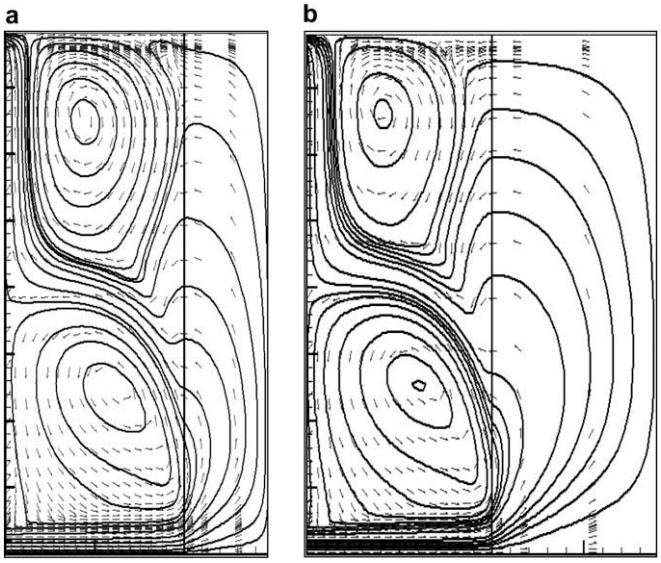

Fig. 11. Effect of porous layer thickness on streamfunction for $H = 0.10$ m, $Re = 30{,}000$ and porous foam G10: (a) $h_p = 0.05$ m, (b) $h_p = 0.10$ m.

a feature substantially different from the single recirculation shown before (Fig. 2). For comparisons, the recirculating bubble closer to cylinder centerline will be called *primary* whereas the one near the cylinder wall will be named *secondary* recirculation. For the present case, both primary and secondary recirculations seem to be slightly larger than those from flow visualizations with LDV, but in general, results seem to be in good agreement with experimental data. The streamlines inside the porous medium cannot be seen by flow visualization methods due to the opaque characteristic of the porous material. They however can be predicted from the flow behavior in the fluid layer above the foam.

The effect of the height of the fluid layer is shown next in Fig. 10, showing the streamfunction behavior for $H = 0.15$, 0.10 and 0.05 m. For $H = 0.15$ m, the primary recirculation is much stronger than the secondary one, indicating a smaller effect of the porous layer on the flow structure in the free flow region. Under such conditions, the flow behavior tends to be similar to that obtained in a cylinder without the porous layer. This happens due to the spread of the jet before colliding into the porous foam. With a decrease in H, the primary recirculation tends to decrease in size as the secondary one grows, so that for $H = 0.10$ m both bubbles have almost the same dimensions, filling almost completely the fluid layer and compressing the streamlines between both recirculations. For $H = 0.05$ m, both recirculations decrease in size, moving their centers apart, towards the cylinder centerline (*primary*) and in the direction of the cylinder wall (*secondary*). Streamlines between both recirculations are distributed rather regularly, with the flow nearly perpendicular to the interface as fluid leaves the porous foam to the fluid layer, a different behavior from that occurring for higher values of H.

The effect of the porous layer thickness, h_p, is presented in Fig. 11 while maintaining the same fluid layer height, H. From the picture, it can be inferred that the thickness of the porous foam has less influence on the main flow behavior in comparison with

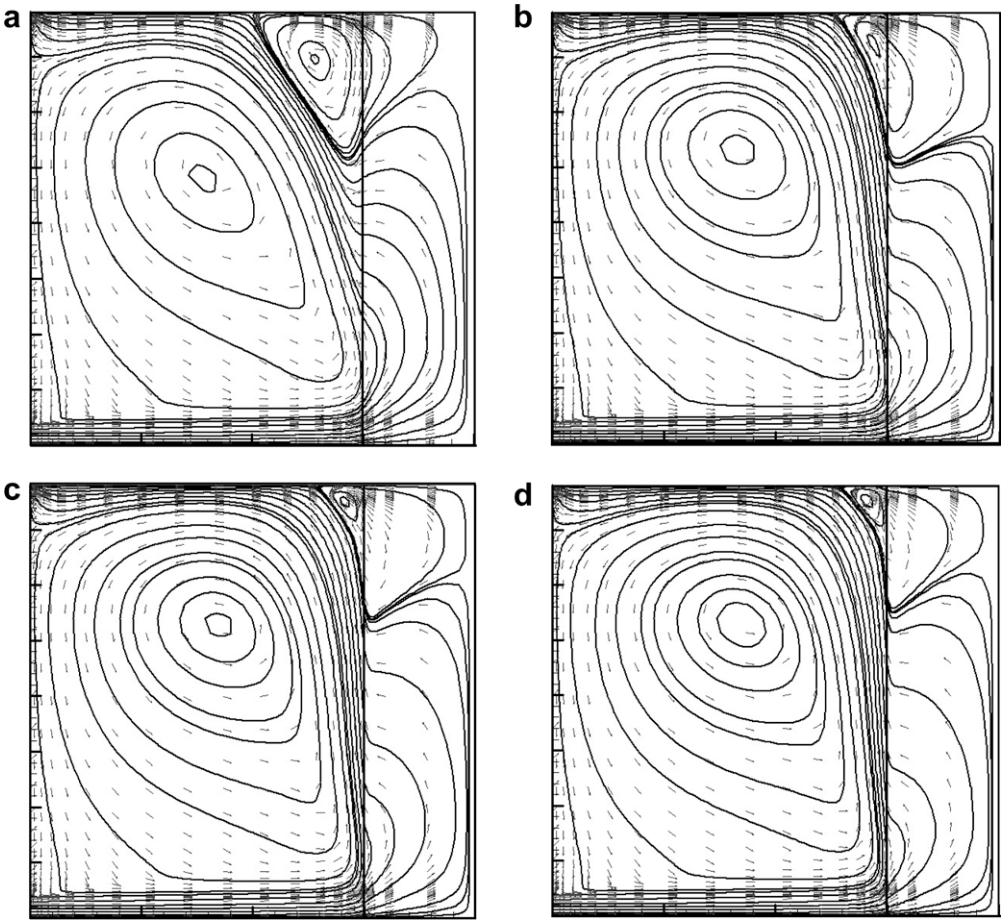

Fig. 12. Effect of porous medium material on streamfunction for $H = 0.15$ m, $h_p = 0.05$ m (see properties in Table 1): (a) G10, (b) G30, (c) G45, (d) G60.

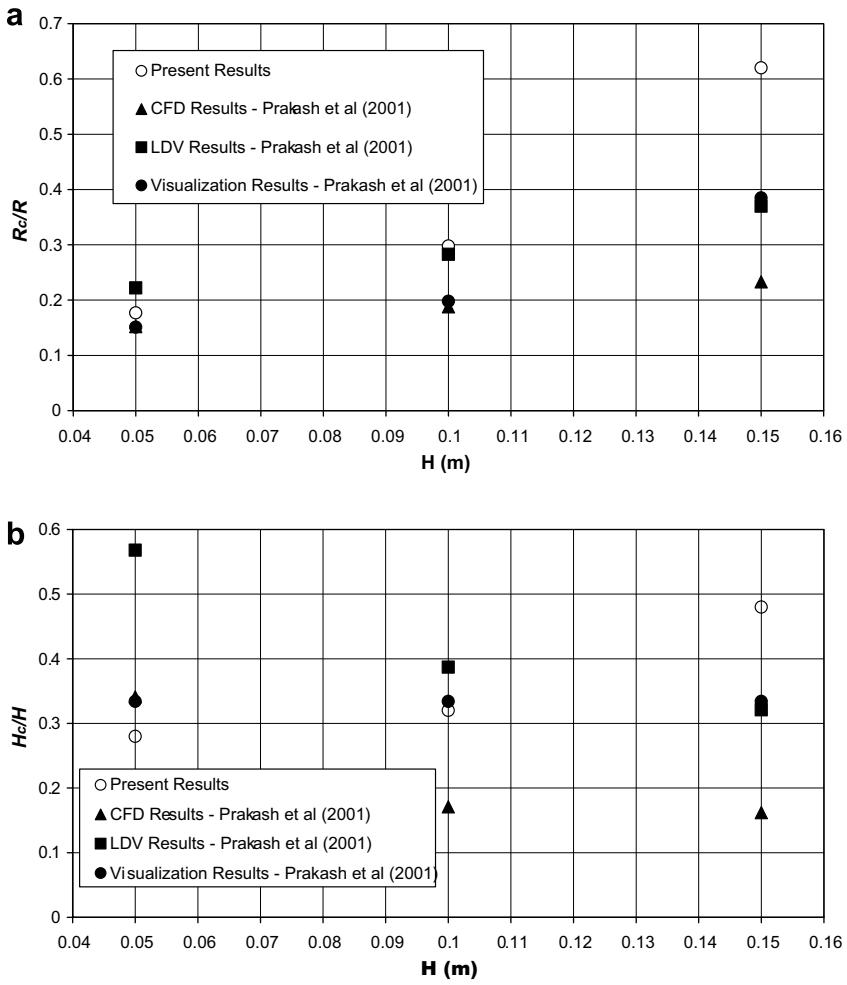

Fig. 13. Position of center of primary recirculation as a function of the height of fluid layer for porous foam G10 and $h_p = 0.05$ m: (a) radial position, (b) axial position.

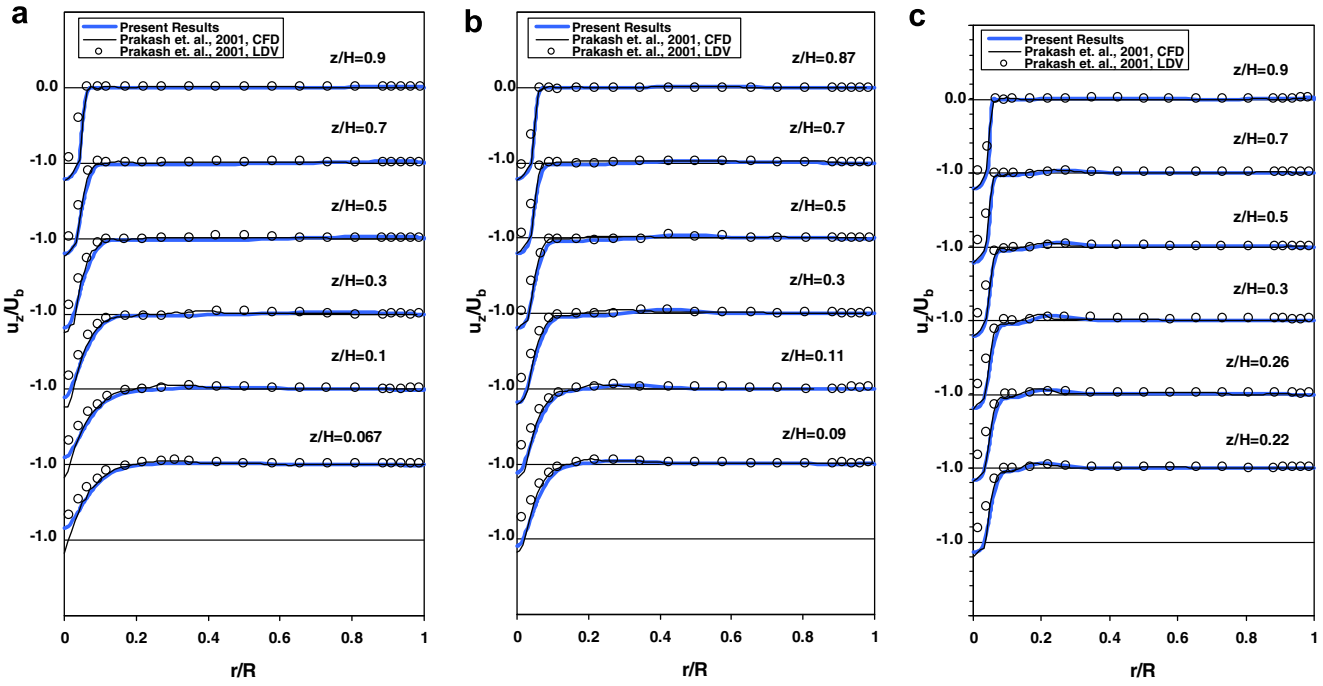

Fig. 14. Axial velocity profiles for $h_p = 0.05$ m on porous foam G10: (a) $H = 0.15$ m, (b) $H = 0.10$ m, (c) $H = 0.05$ m.

the effect caused by varying H (see Fig. 10) With an increase in h_p, the primary recirculation shows only a small increase in size while the secondary one decreases a little. No other significant effect can be detected.

The effect of the porous layer material, effectively representing a change in its permeability, is shown in Fig. 12. For the porous foam G10 (highest permeability), a secondary recirculation develops with considerable size close to the cylinder wall. For the other foams G30, G45 and G60, this recirculation decreases due to the reduction of the porous layer permeability, so that the porous layer tends to act as a solid obstacle being hit by a jet, as in the previous cases presented in Figs. 2, 3, and 5.

Fig. 13 shows radial and axial position of central recirculation (close to the symmetry axis) for porous foam G10 with $h_p = 0.05$ m. From the pictures, a pattern can be distinguished, where the radial position (Fig. 13a) of the recirculation tends to move in the direction of the cylinder wall for an increase in. Although the results are reasonably good for smaller values of,

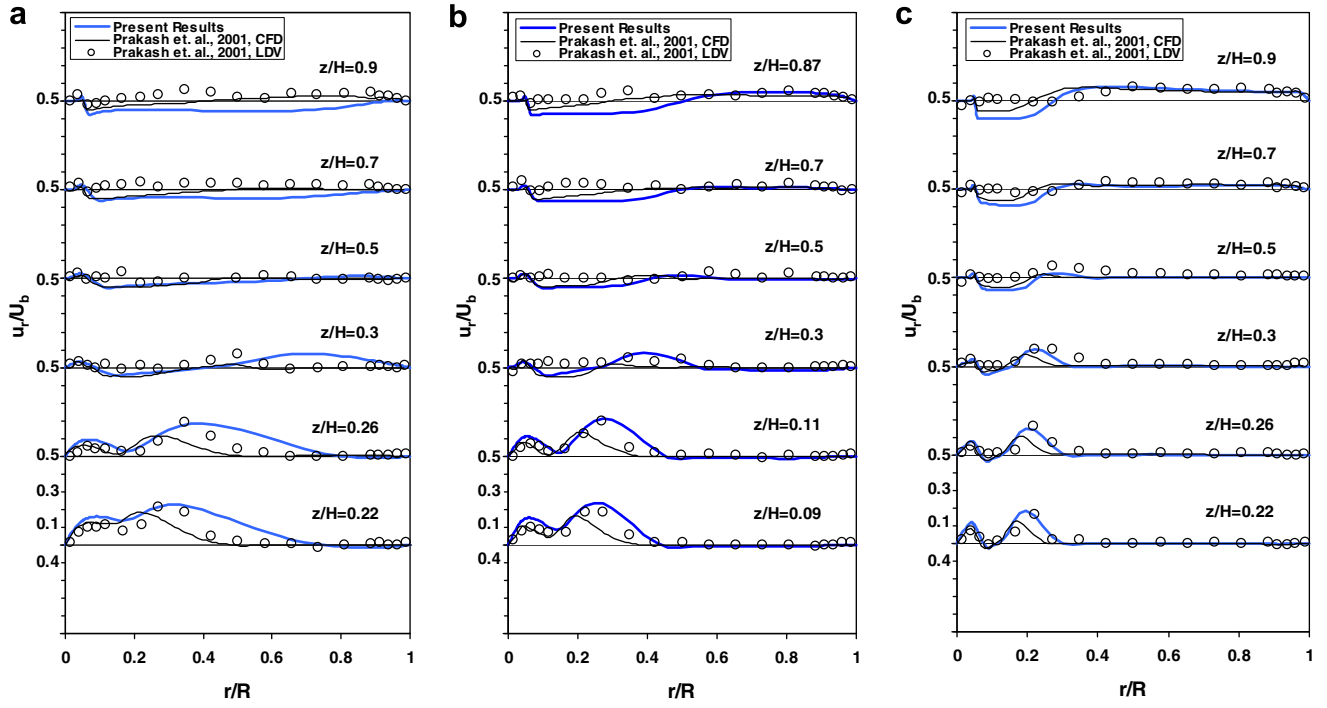

Fig. 15. Radial velocity profiles for h_p= 0.05 m on porous foam G10: (a) H = 0.15 m, (b) H = 0.10 m, (c) H = 0.05 m.

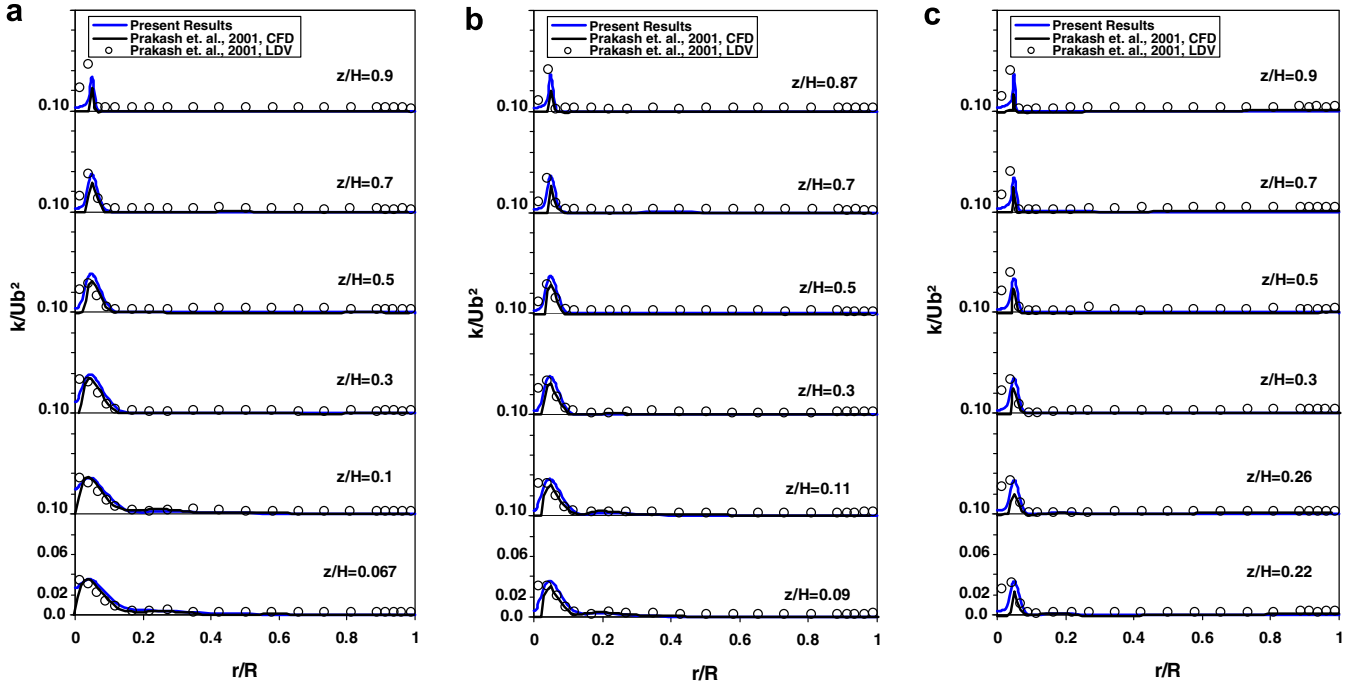

Fig. 16. Turbulence kinetic energy profiles for h_p= 0.05 m on porous foam G10: (a) H = 0.15 m, (b) H = 0.10 m, (c) H = 0.05 m.

simulation behavior for the higher values of H does not satisfactorily represent the central recirculation position along the radial axis. For the axial position (Fig. 13b), another pattern can be noticed. While the LDV measurements indicates a movement of the circulation center in the direction to the collision plate, as H increases, simulations show movement in the opposite direction. Experimental measurements and present results shows a very good agreement for $H = 0.1$ m, but rather poor agreement for $H = 0.05$ m and $H = 0.15$ m. This could be due to mesh sensitivity, with the mesh for $H = 0.1$ m representing an optimal grid point distribution for that specific case. In fact, optimal grid distribution was investigated only for the case $H = 0.1$ m whereas for $H = 0.05$ and $H = 0.15$ the same grid layout was applied.

Results for the axial velocity profiles are shown in Fig. 14, for porous foam G10 and $h_p = 0.05$ m and $Re = 30{,}000$. For all three fluid layers, it can be seen that both numerical simulations seems to slightly overpredict the actual flow behavior close to the jet centerline. For $H = 0.15$ m, numerical predictions are closer to experimental data in comparisons with $H = 0.10$ and 0.05 m. The general over prediction of the velocities profiles might be due to the fact that, in the experiments, the flow at the jet exit was not fully developed, a condition which was assumed in the simulations here reported. Fig. 15 presents the radial profiles for the same parameters as in the previous figure. For higher values of z/H, simulations seem to present difficulties in following experimental data, even though, close to the interface region, the flow behavior is reasonably well predicted, particularly for $H = 0.10$ m. For the second hump along radial profiles, while numerical simulations by Prakash et al. [21,22] under predict experimental values, simulations herein over predicts them by a small amount.

8.2. Turbulent field

Turbulence kinetic energy profiles are shown in Fig. 16. As in the case of clear medium (Fig. 8), results give a good prediction for the profiles, following closely the peak value of turbulent en-

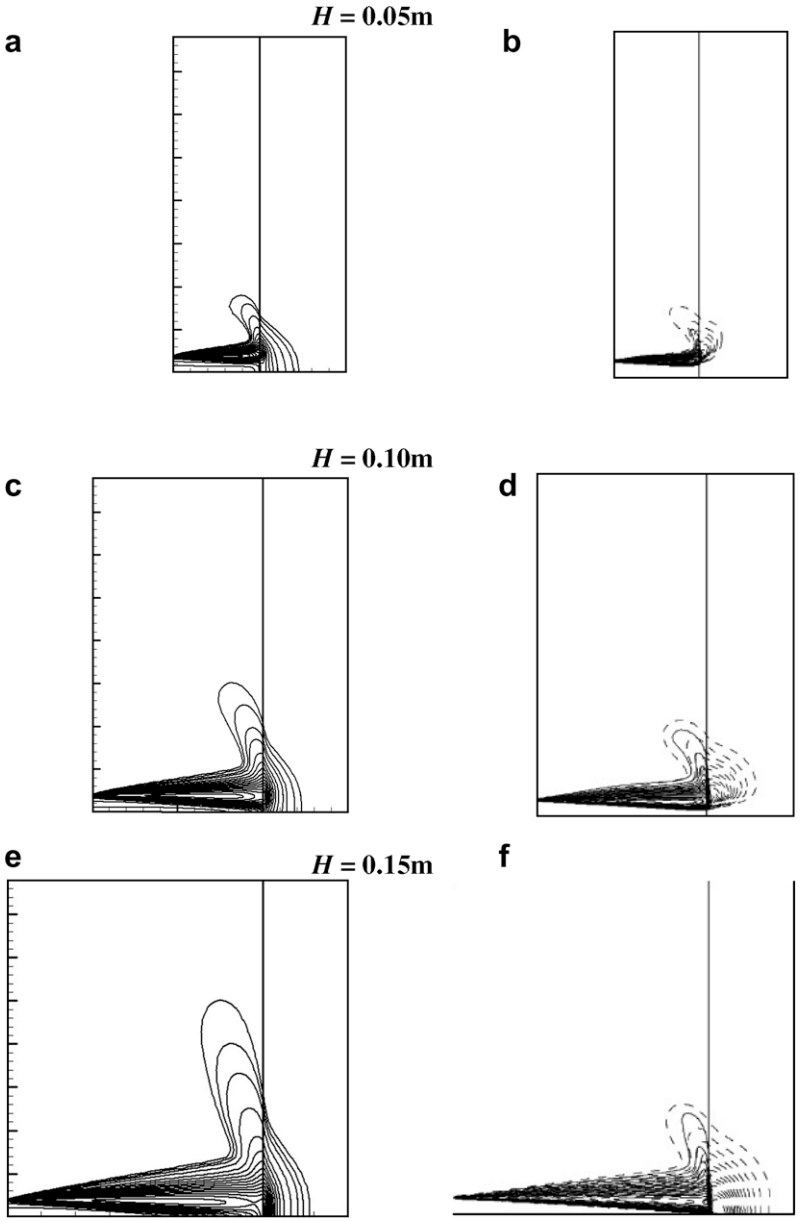

Fig. 17. Comparison of turbulence kinetic energy contours for $h_p = 0.05$ m on porous foam G10: Left: (a, c, d) Present Results, Right: (b, d, e) CFD simulations – Prakash et al. (2001) where: **Dashed Lines** – Darcy term only, **Solid lines** – Darcy & Forchheimer terms.

ergy close to the cylinder central axis. Finally, Fig. 17 shows turbulent kinetic energy contours for h_p = 0.05 m, porous foam G10 and *Re* = 30,000. From the picture, it can be seen that turbulence penetrates into the porous medium, as can be noticed by the contour lines that goes inside the porous bed. As the jet penetrates the foam, calculated turbulence intensities with this model seem to be lower than those by Prakash et al. [21,22], who used only the Darcy term (dashed lines in Fig. 17b–d–f). However, calculated levels of turbulence herein are higher than those computed by the same authors using both the Darcy and Forchheimer terms (solid lines). This second set of results by Prakash et al. [21,22] indicates that turbulence is damped almost completely at the interface. At the fluid layer, results are in agreement with published data.

9. Conclusions

Numerical simulations were carried out for the flow field formed by a jet crossing a fluid layer and impinging onto a surface covered with a porous material. Turbulence was handled with a macroscopic k-ε model, which uses the same set of equations for both the fluid layer and the porous matrix. The numerical technique employed is the control volume method in conjunction with a boundary-fitted coordinate system. One unique computational grid was used to compute the entire heterogeneous medium. Effects of porous material type, fluid layer height, porous layer thickness and Reynolds number on the flow pattern were presented. Since the porosity for all foams simulated was very close do unity, changes in the foam material were representative of changes in their permeability. It was observed that the permeability of the porous layer and the height of the fluid layer significantly affect the flow pattern. The effect of the porous layer thickness was less pronounced. Further, the influence of the Reynolds number on the flow behavior was small. Finally, comparisons with available data in the literature seem to indicate that the turbulence model applied here described the turbulence phenomena inside the porous medium with similar degree of accuracy of that of articles published in the open literature.

Acknowledgments

The authors are thankful to CNPq and FAPESP, Brazil, for their financial support during the course of this research.

References

[1] H.S. Law, H.M. Jacob, Numerical prediction of the flow field due to a confined laminar two-dimensional submerged jet, Computers & Fluids 12 (3) (1984) 199–215.
[2] E. Baydar, Confined impinging air jet at low reynolds numbers, Experimental Thermal and Fluid Science 19 (1999) 27–33.
[3] R. Chalupa, M. Chen, A.C. West, V. Modi, High schmidt mass transfer in a turbulent impinging slot jet, International Journal of Heat and Mass Transfer 44 (2001) 3775–3785.
[4] T.H. Park, H.G. Choi, J.Y. Yoo, S.J. Kim, Streamline upwind numerical simulation of two-dimensional confined impinging slot jets, International Journal of Heat and Mass Transfer 46 (2003) 251–262.
[5] K. Vafai, S.J. Kim, Analysis of surface enhancement by a porous substrate, Journal of Heat Transfer 112 (1990) 700–706.
[6] P.C. Huang, K. Vafai, Flow and heat transfer control over an external surface using a porous block array arrangement, International Journal of Heat and Mass Transfer 36 (1993) 4019–4032.
[7] A. Hadim, Forced convection in a porous channel with localized heat sources, Journal of Heat Transfer 116 (1994) 465–472.
[8] Y. Zhang, X.F. Peng, I. Conte, Heat and mass transfer with condensation in non-saturated porous media, Numerical Heat Transfer Part A – Applications 52 (2007) 1081–1100.
[9] M.E. Taskin, A.G. Dixon, E.H. Stitt, CFD study of fluid flow and heat transfer in a fixed bed of cylinders, Numerical Heat Transfer Part A – Applications 52 (3) (2007) 203–218.
[10] T. Basak, S. Roy, H.S. Takhar, Effects of nonuniformly heated wall(s) on a natural-convection flow in a square cavity filled with a porous medium, Numerical Heat Transfer Part A – Applications 51 (10) (2007) 959–978.
[11] V. Bubnovich, L. Henriquez, N. Gnesdilov, Numerical study of the effect of the diameter of alumina balls on flame stabilization in a porous-medium burner, Numerical Heat Transfer Part A – Applications 52 (3) (2007) 275–295.
[12] X.B. Chen, P. Yu, S.H. Winoto, H.T. Low, Free convection in a porous wavy cavity based on the Darcy–Brinkman–Forchheimer extended model, Numerical Heat Transfer Part A – Applications 52 (4) (2007) 377–397.
[13] N. Yucel, R.T. Guven, Forced-convection cooling enhancement of heated elements in a parallel-plate channels using porous inserts, Numerical Heat Transfer Part A – Applications 51 (3) (2007) 293–312.
[14] J. Eriksson, S. Ormarsson, H. Petersson, Finite-element analysis of coupled nonlinear heat and moisture transfer in wood, Numerical Heat Transfer Part A – Applications 50 (9) (2006) 851–864.
[15] L. Betchen, A.G. Straatman, B.E. Thompson, A nonequilibrium finite-volume model for conjugate fluid/porous/solid domains, Numerical Heat Transfer Part A – Applications 49 (6) (2006) 543–565.
[16] Y.W. Zhang, Nonequilibrium modeling of heat transfer in a gas-saturated powder layer subject to a short-pulsed heat source, Numerical Heat Transfer Part A – Applications 50 (6) (2006) 509–524.
[17] A. Mansour, A. Amahmid, M. Hasnaoui, M. Bourich, Multiplicity of solutions induced by thermosolutal convection in a square porous cavity heated from below and submitted to horizontal concentration gradient in the presence of Soret effect, Numerical Heat Transfer Part A – Applications 49 (1) (2006) 69–94.
[18] A.V. Kuznetsov, L. Cheng, M. Xiong, Effects of thermal dispersion and turbulence in forced convection in a composite parallel-plate channel: investigation of constant wall heat flux and constant wall temperature cases, Numerical Heat Transfer Part A – Applications 42 (4) (2002) 365–383.
[19] B.M.D. Miranda, N.K. Anand, Convective heat transfer in a channel with porous baffles, Numerical Heat Transfer Part A – Applications 46 (5) (2004) 425–452.
[20] N.B. Santos, M.J.S. de Lemos, Flow and heat transfer in a parallel-plate channel with porous and solid baffles, Numerical Heat Transfer Part A – Applications 49 (5) (2006) 471–494.
[21] M. Prakash, F.O. Turan, Y. Li, J. Manhoney, G.R. Thorpe, Impinging round jet studies in a cylindrical enclosure with and without a porous layer. Part I: flow visualizations and simulations, Chemical Engineering Science 56 (2001) 3855–3878.
[22] M. Prakash, F.O. Turan, Y. Li, J. Manhoney, G.R. Thorpe, Impinging round jet studies in a cylindrical enclosure with and without a porous layer. Part II: DLV measurements and simulations, Chemical Engineering Science 56 (2001) 3879–3892.
[23] W.-S. Fu, H.-C. Huang, Thermal performance of different shape porous blocks under an impinging jet, International Journal of Heat and Mass Transfer 40 (10) (1997) 2261–2272.
[24] S.Y. Kim, A.V. Kuznetsov, Optimization of pin-fin heat sinks using anisotropic local thermal nonequilibrium porous model in a jet impinging channel, Numerical Heat Transfer Part A – Applications 44 (8) (2003) 771–787.
[25] N.H. Saeld, Jet impingement interaction with cross flow in horizontal porous layer under thermal non-equilibrium conditions, International Journal of Heat and Mass Transfer 50 (21–22) (2007) 4265–4274.
[26] W.P. Jones, B.E. Launder, The prediction of laminarization with a two-equation model of turbulence, International Journal of Heat and Mass Transfer 15 (1972) 301–314.
[27] M.H.J. Pedras, M.J.S. de Lemos, Macroscopic turbulence modeling for incompressible flow through undeformable porous media, International Journal of Heat and Mass Transfer 44 (6) (2001) 1081–1093.
[28] M.H.J. Pedras, M.J.S. de Lemos, Computation of turbulent flow in porous media using a low-Reynolds k-epsilon model and an infinite array of transversally displaced elliptic rods, Numerical Heat Transfer Part A – Applications 43 (6) (2003) 585–602.
[29] M.J.S. de Lemos, Turbulent kinetic energy distribution across the interface between a porous medium and a clear region, International Communication of Heat and Mass Transfer 32 (1–2) (2005) 107–115.
[30] M.J.S. de Lemos, R.A. Silva, Turbulent flow over a layer of a highly permeable medium simulated with a diffusion-jump model for the interface, International Journal of Heat and Mass Transfer 49 (3–4) (2006) 546–556.
[31] D.R. Graminho, M.J.S. de Lemos, Laminar confined impinging jet into a porous layer, Numerical Heat Transfer Part A – Applications 54 (2) (2008) 151–177.
[32] F.D. Rocamora Jr, M.J.S. de Lemos, Analysis of convective heat transfer of turbulent flow in saturated porous media, International Communication of Heat and Mass Transfer 27 (6) (2000) 825–834.
[33] M.J.S. de Lemos, F.D. Rocamora, Turbulent transport modeling for heated flow in rigid porous media, Proceedings of the 12th International Heat Transfer Conference, Grenoble, France, August 18–23, 2002, pp. 791–795.
[34] M.J.S. de Lemos, E.J. Braga, Modeling of turbulent natural convection in saturated rigid porous media, International Communication of Heat and Mass Transfer 30 (5) (2003) 615–624.
[35] E.J. Braga, M.J. S de Lemos, Turbulent natural convection in a porous square cavity computed with a macroscopic k-ε model, International Journal of Heat and Mass Transfer 47 (26) (2004) 5639–5650.
[36] E.J. Braga, M.J.S. de Lemos, Heat Transfer in Enclosures Having a Fixed Amount of Solid Material Simulated with Heterogeneous and Homogeneous Models, International Journal of Heat and Mass Transfer 48 (23–24) (2005) 4748–4765.
[37] E.J. Braga, M.J. S de Lemos, Laminar Natural Convection in Cavities Filled with Circular and Square Rods, International Communication of Heat and Mass Transfer 32 (10) (2005) 1289–1297.

[38] E.J. Braga, M.J.S. de Lemos, Turbulent heat transfer in an enclosure with a horizontal porous plate in the middle, Journal of Heat Transfer 128 (2006).
[39] E.J. Braga, M.J.S. de Lemos, Simulation of turbulent natural convection in a porous cylindrical annulus using a macroscopic two-equation model, International Journal of Heat and Mass Transfer 49 (23–24) (2006) 4340–4351.
[40] E.J. Braga, M.J.S. de Lemos, Computation of turbulent free convection in left and right tilted porous enclosures using a macroscopic k-ε model, International Journal of Heat and Mass Transfer 51 (21–22) (2008) 5279–5287.
[41] E.J. Braga, M.J.S. de Lemos, Laminar and Turbulent Free Convection in a Composite Enclosure, International Journal of Heat and Mass Transfer 52 (3–4) (2009) 588–596.
[42] M.J.S. de Lemos, M.S. Mesquita, Turbulent mass transport in saturated rigid porous media, International Communication of Heat and Mass Transfer 30 (1) (2003) 105–113.
[43] M.J.S. de Lemos, L.A. Tofaneli, Modeling of double-diffusive turbulent natural convection in porous media, International Journal of Heat Mass Transfer 47 (19–20) (2004) 4221–4231.
[44] M. Assato, M.H.J. Pedras, M.J.S. de Lemos, Numerical solution of turbulent channel flow past a backward-facing-step with a porous insert using linear and non-linear k-ε models, Journal of Porous Media 8 (1) (2005) 13–29.
[45] M.J.S. de Lemos, Analysis of turbulent flows in fixed and moving permeable media, Acta Geophysica 56 (3) (2008) 562–583.
[46] M.J.S. de Lemos, Turbulent kinetic energy in a moving porous bed, International Communications in Heat and Mass Transfer 35 (9) (2008) 1049–1052.
[47] W.G. Gray, P.C.Y. Lee, On the theorems for local volume averaging of multiphase system, International Journal of Multiphase Flow 12 (1977) 401–410.
[48] S.V. Patankar, Numerical Heat Transfer and Fluid Flow, Hemisphere, New York, 1980.
[49] B.V. Antohe, J.L. Lage, A general two-equation macroscopic turbulence model for incompressible flow in porous media, International Journal of Heat and Mass Transfer 40 (1997) 3013.
[50] M.J.S. de Lemos, Fundamentals of the double – decomposition concept for turbulent transport in permeable media, Materialwissenschaft und Werkstofftechnik 36 (10) (2005) 586–593.
[51] B.E. Launder, D.B. Spalding, The numerical computation of turbulent flows, Comparative Methods in Applied Mechanical Engineering 3 (1974) 269–289.
[52] F.P. Incropera, D.P. DeWitt, Fundamentals of Heat and Mass Transfer, Wiley, New York, 1990.